Applied Physics A (2021) 127:390
https://doi.org/10.1007/s00339-021-04501-0

Applied Physics A
Materials Science & Processing

Structural, spectroscopic and electrical properties of dc magnetron sputtered NiO thin films and an insight into different defect states

Parashurama Salunkhe[1] · Muhammed Ali A.V[1] · Dhananjaya Kekuda[1]

Received: 31 December 2020 / Accepted: 8 April 2021 / Published online: 29 April 2021
© The Author(s) 2021

Abstract

In this article, we report a detailed study on the influence of sputter power on physical properties of the NiO films grown by DC magnetron sputtering. Structural studies carried out by Grazing Incidence X-ray diffraction (XRD) reveals the polycrystalline nature of the films with FCC phase. The crystallographic orientation (111) plane followed by (200), (220), and (311) plane were evident from the XRD spectra. The average crystallites sizes were estimated from the spectra, and the values were compared using three different plots such as Scherrer, Williamson–Hall and size–strain plot. The surface morphology was carried out by atomic force microscopy. The deposited samples show semitransparent behavior in the visible region and the estimated band gap increased from 2.70 to 3.34 eV with an increase in sputter power. Furthermore, X-ray photoelectron spectroscopy (XPS) core-level Ni2p spectra were deconvoluted and the observed $Ni2p_{3/2}$, $Ni2p_{1/2}$ domain along with their satellite's peaks were analyzed. Most importantly, XPS quantification data and Raman spectra confirm the presence of both Ni^{2+} and Ni^{3+} states in the NiO films. The electrical properties carried at room temperature revealed that the resistivity of the film significantly increased and a mobility of ~ 84 $cm^2V^{-1}s^{-1}$ was obtained.

Keywords NiO · Sputtering · XPS · Ni2p-O1s spectra · Ni^{2+} and Ni^{3+} state · Raman spectroscopy

1 Introduction

Semiconductor device industries rapidly expanded in recent years and it largely relies on the advanced thin film technology with functional materials for microelectronics applications. Nowadays, variety of metal oxide gained much attention due to their inherent physical properties. In the last few decades, transparent conducting oxides (TCOs) were studied extensively and the mutual existence of both electrical conductivity and optical transparency in a visible domain attracted them for several applications which include transparent thin film transistors, organic and inorganic light-emitting diode, solar cells, flat panel display, etc.[1–3]. Basically, TCOs and most of the oxide semiconductors exhibited wide band gap, and to understand the functionalities it is essential to study the interaction between the metal–oxygen bonding in the lattice [4]. Generally accepted TCOs from the research community include tin oxide (SnO_x), indium tin oxide (ITO), copper oxide (CuO_x), zinc oxide (ZnO), fluorine-doped tin oxide (FTO), nickel oxide (NiO), etc. [5–8]. Majority of the research work has focused on n-type TCOs due to their excellent stability and electrical performance. Although the reports are available on p-type TCOs such as CuO_x and SnO_x, the main obstacle of these materials is the degrading issues. Moreover, their physical properties vary drastically since they react with the atmosphere elements such as air, humidity [9]. Overall, to explore physical, chemical and electrical properties of a p-type material are still lagging.

Among the transition metal oxides, nickel oxide (NiO) is an interesting p-type material owing to its chemical and mechanical suitability for transparent devices. NiO has a unique functional property like hole transport ability and gas sensing, etc.[10–12]. Besides, NiO thin film possess wide band gap varying from 3.2 to 3.6 eV. It has a cubic crystal structure, which is almost close to that of NaCl (rock salt structure). The material has shown extreme stability at wide range of temperatures [13]. Interestingly, NiO is one of the less toxic materials compared to other transition semiconductor materials [14].

✉ Dhananjaya Kekuda
dhaya.kekuda@manipal.edu

[1] Department of Physics, Manipal Institute of Technology, Manipal Academy of Higher Education, Manipal 576104, India

Magnetron sputtering has been one of the physical deposition methods for achieving high-quality thin films. Majority of the articles reported NiO thin films were grown by using various techniques which include spray pyrolysis, spin coating, radio frequency sputtering, and DC magnetron sputtering [10, 15–17]. Among these methods, DC magnetron sputtering provides uniform coverage of the deposits, control over the stoichiometry of the desired compound, and it is a commercially viable technique. One of the variances of this technique is the reactive DC magnetron sputtering in which reactive gas partial pressure and sum of total sputtering pressure significantly plays an important role in getting desired films [18]. Moreover, post-annealing treatment, substrate temperature, the distance between target to the substrate, etc., may impact the microstructural properties of the growing films. Therefore, specifically controlling these parameters is essential during deposition. Among these, the influence of sputtered power on various defect states in NiO thin films through reactive DC magnetron sputtering is not explored much. The formation of different defects states in the interface can play crucial role for device applications. The present work provides an insight into the importance of various defects states, interaction between the nickel–oxygen atoms, and examine the effect of sputter power on other physical properties of NiO thin films.

2 Experimental details

NiO thin films were grown on glass substrates by reactive DC magnetron sputtering. In this process, we have used a two-inch circular Ni target (99.99% purity). The distance between the target and the substrate was around 75 mm. The substrates were cleaned with DI water followed by ultrasonication in acetone and isopropyl alcohol for about 10 min and dried with the nitrogen gas. Finally, these substrates were exposed under UV ozone treatment for 15 min and then loaded to the sputter chamber. The deposition chamber base pressure was maintained approximately at $7X10^{-4}$ Pa. The deposition process was carried out at a partial pressure of 1Pascal.

in Argon and Oxygen atmosphere with the ratio of 2:1 at room temperature with varying sputter powers. The target was initially pre-sputtered for about 10 min to eliminate the contamination on the surface of the target. Both gas flow rate individually controlled by mass flow controllers (Bronkhorst High-Tech, MFC). The sputtering power was varied from 30 to 70 W at a step of 10 W during sputtering. During this process, sputtering yield has varied and to maintain a film thickness of 204 ± 4 nm for all the samples, the time of deposition for the individual depositions was varied. Furthermore, silver electrodes were deposited on the top of the NiO film by thermal evaporation method using shadow mask. The maintained deposition rate was 5 Å/*s* and a 80 nm thickness was monitored by quartz crystal oscillator.

3 Characterizations

Thickness of the grown NiO thin films was measured through the stylus profilometer (DektakXT-Bruker). The structural properties such as phase and preferred orientations of the samples was analyzed by Grazing Incidence X-ray diffractometer (GXRD)–(Rigaku, Cu Kα λ = 1.5405 Å), with scan rate maintained at 5° per minute and 2θ ranging from 20–80°. The surface morphology of all the samples was studied by an atomic force microscope (AFM-park smart scan system) with a tapping mode configuration. The transmittance and absorbance spectra of the films were recorded by UV—Visible spectrophotometer over the range of 190 to 1000 nm (Shimadzu UV-1800). X-ray photoelectron spectroscopy was used to confirm the oxidation state and extract their chemical composition (XPS, Axis ultra DLD – Kratos analytical). Monochromatic Al K_{α} X-rays (1486.69 eV) as an excitation source for XPS. The Raman spectra was used to confirm the different modes of the NiO thin films (Horiba JOBINYVON LabRAM HR). To investigate the electrical properties, Keithley Hall effect measurements in Van der Pauw configurations were used, and the measurements were done at room temperature under a 0.6 T magnetic field.

4 Results and discussion

4.1 Structural analysis

The crystallographic structure and intrinsic strain in the NiO thin films were investigated by grazing incidence X-ray diffractometer (GXRD). Figure 1 represents the X-ray diffraction spectra of grown NiO thin films which confirms the polycrystalline nature of the samples, and the resultant spectrum peaks observed as per the indexed standard JCPDS (data No. 03–065- 2901) file. XRD confirmed that patterns exhibited cubic polycrystalline structure with the FCC phase, space group of Fm-3 m (225). The obtained XRD spectra exhibited four Bragg reflection peaks such as (111), (200), (220), (311) and (222) located at 37.08°, 42.43°, 62.50°, and 75.26°, and 79.23 °, respectively. It can be observed that there were no additional XRD peaks corresponding to secondary phases present in the spectra [19]. At a diffraction angle, 2θ located at 37.08°, a strong (111) preferred orientation was observed. Generally, (111) plane has densely packed atoms with NiO thin film.

has mutually combined Ni^{2+} and O^{2-} on the substrate. Hence, atoms are arranged in (111) preferred oriented plane

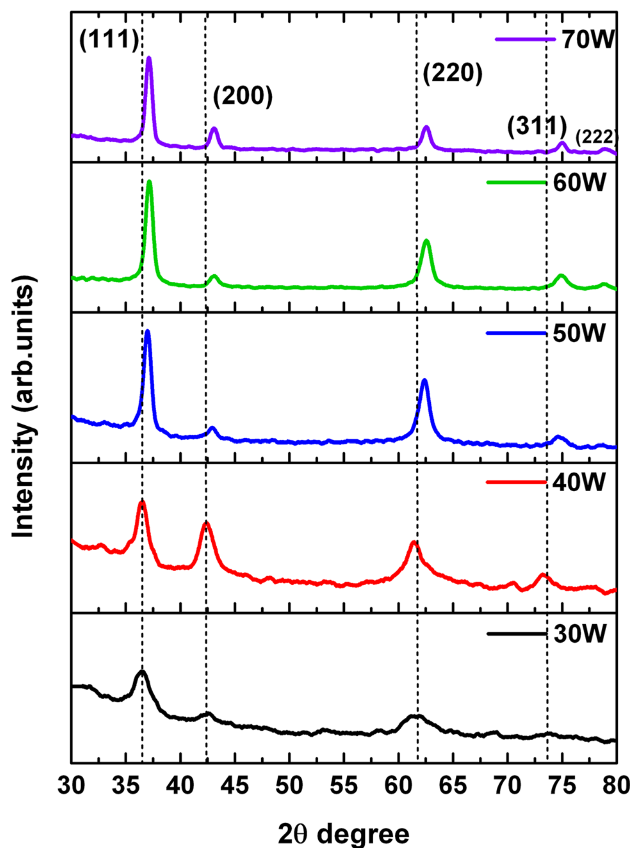

Fig. 1 XRD spectrum of NiO thin films at different sputter powers

followed by (200), (220), (311), and (222) planes to minimize the surface energy [20].

Figure 1 shows that the diffraction peaks slightly shifted toward a higher angle with increasing sputter power. It could be ascribed to the presence of the lattice strain in the film, and also it can be found that there was an expansion in the lattice parameter listed in Table 1. Such variation in the lattice parameter is associated with the changes in the dislocation density from 26.26×10^{15} m^{-2} to 6.84×10^{15} m^{-2} of the atoms in the films [21]. Also, observed that the intensity of all the diffraction peaks was minimal for the films grown at lower sputter powers, and it drastically increased after 50 W of sputter power, as depicted in Fig. 1. At low sputter powers, the number of ejected Ni atoms is less from the Nickel target due to low sputtering yield. On the other hand, at higher sputter powers intensive ion bombardment usually activates the deposition process. Growing thin film at higher sputter power helps the adatoms to gain additional kinetic energy and deposited Ni^{2+} and O^{2-} ions rearrange on the substrate to form a desired crystalline structure [20].

We have estimated the average crystallite size of the NiO film, which has shown an increasing trend with increase in the sputter power. The crystallite size increased from 6.17 to 12.09 nm as the sputter power changed from 30 to 70 W. The poor crystallinity of the film deposited at low sputter power could be attributed to the segregation of oxygen during deposition process.

4.1.1 Scherrer method

The peak broadening (β) observed in the XRD spectra gives a measure of various structure parameters such as crystallite size and dislocation density. The crystallites size of the NiO thin film was calculated by using Scherrer equation.

$$\mathrm{D} = \frac{0.9\lambda}{\beta \mathrm{Cos}\theta} \tag{1}$$

where D is crystallite size, λ is the wavelength of the X-ray radiation (1.54Å for Cu K_{α}), β is the full-width half maxima, and θ is the diffraction angle. The calculated average crystallite size was found to increase from 6.17 to12.1 nm with the increase in the sputter power. Dislocation density was calculated by using the following relation:

$$\delta = \frac{1}{\mathrm{D}^2} \tag{2}$$

where D is the grain size of the film. The inverse relationship of the crystallite size and the dislocation density suggest that δ in the films was found to decrease from 26.3×10^{15} / m^2 to 6.84×10^{15} /m^2. One of the basic requirements for the applicability of these films in the device applications is to grow films with better crystallinity and reduced dislocation

Table 1 Physical parameters extracted from the NiO thin films deposited at different sputter powers

Sputter power (W)	Average crystallite size (nm) (Scherrer)	Dislocation density (10^{15} /m^2)	Number of crystallites (10^{16} /m^2)	Thickness (nm)	Lattice parameter (Å)	Optical Band gap (eV)	Roughness (nm)
30	6.17	26.26	85.14	200	4.25	2.70	2.20
40	7.68	16.95	45.25	205	4.25	3.25	1.72
50	10.56	8.96	17.15	202	4.20	3.34	2.00
60	10.66	8.88	16.67	202	4.24	3.14	1.00
70	12.09	6.84	11.77	208	4.22	3.33	1.20

density. The structural and physical properties of NiO thin films are listed in Table 1.

4.1.2 Williamson–hall (W–H) plot

The W–H plot is useful to extract the crystallite size along with the microstrain in the NiO films with the help of the following equations [22].

$$\beta_{\mathrm{hkl}} = \beta_S + \beta_D \tag{3}$$

$$\beta_{\mathrm{hkl}} = \frac{K\lambda}{D\ \cos\theta} + 4\varepsilon\ \tan\theta \tag{4}$$

$$\beta_{\mathrm{hkl}}\ \cos\theta = \frac{K\lambda}{D} + 4\varepsilon\ \sin\theta \tag{5}$$

$$\varepsilon = \frac{\beta\cos\theta}{4\sin\theta} \tag{6}$$

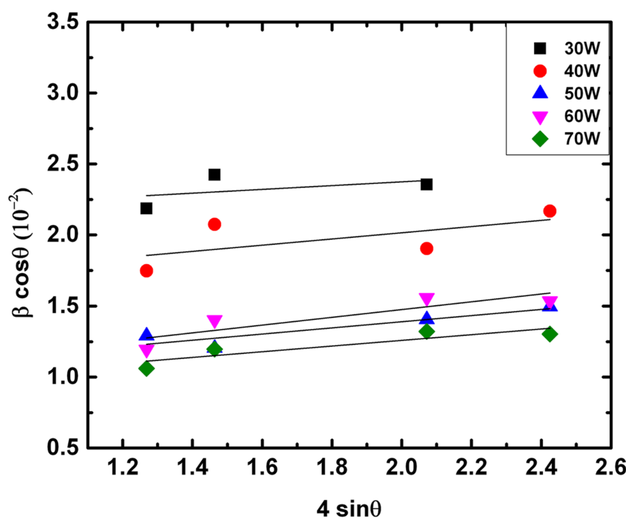

Fig. 2 Williamson–Hall (W–H) plots for NiO thin films deposited at different sputter powers

A plot of $\beta_{\mathrm{hkl}}\cos\theta$ versus $4\sin\theta$ is shown in Fig. 2. The Y- intersection is a measure of the crystallite size and the strain can be estimated from the slope of the fitted line. As shown in Fig. 2, it contained all W–H plots of NiO thin films deposited at different sputter power, and evaluated values were tabulated in Table 2.

4.1.3 Size–strain (S–S) plot

SS plot is one of the methods to find the detailed peak analysis, and it gives the microstructure contribution and average crystallite size from the XRD spectra.

$$\beta_{\mathrm{hkl}} = \beta_L + \beta_G \tag{7}$$

where β_L broadening due to Lorentzian function β_G broadening due to Gaussian function

$$\left(d_{\mathrm{hkl}}\beta_{\mathrm{hkl}}\cos\theta\right)^2 = \frac{k}{D}\left(d_{\mathrm{hkl}}^2\beta_{\mathrm{hkl}}\cos\theta\right) + \left(\frac{\varepsilon}{2}\right)^2 \tag{8}$$

where $d = \sqrt{\frac{a^2}{h^2+k^2+l^2}}$ and k is the shape factor.

The SS plot of $\left(d_{\mathrm{hkl}}\beta_{\mathrm{hkl}}\cos\theta\right)^2$ versus $\left(d_{\mathrm{hkl}}^2\beta_{\mathrm{hkl}}\cos\theta\right)$ for 2θ values ranging from 30 to 80° for NiO thin films grown at different sputter powers is shown in Fig. 3. In this case, the crystallite size of the film is estimated from the slope of the fitted curves and strain can be estimated from the square root of the y-intercept. We have analyzed the XRD data using three different methods, and the comparison of extracted structural parameters is listed in Table 2.

4.2 Surface morphology

The surface morphology of the NiO thin films was carried out by atomic force microscopy with a scan area range of 1 µm x 1 µm and is shown in Fig. 4. Notably, texture of all samples was densely packed, and the grains are uniformly distributed all over the surface. The surface roughness of the NiO films was evaluated by using Gwydion software and the extracted parameters are listed in Table 1. The deposited NiO thin films at 30 W sputter power showed surface roughness value of 2.20 nm. At low sputter powers such as 30 W,

Table 2 Comparison of NiO thin films average crystallite size and strain with different sputter powers

Sputter power (W)	Scherrer equation	Williamson-hall plot		Size-strain plot	
	crystallites size (nm)	Crystallites size (nm)	Strain (ε) X 10^{-3}	Crystallites size (nm)	Strain (ε) X 10^{-3}
30	6.17	6.89	1.39	6.64	11.48
40	7.68	9.20	2.24	7.90	2.89
50	10.56	15.14	2.17	13.80	12.94
60	10.66	15.62	2.77	15.50	16.55
70	12.09	16.83	2.01	16.23	11.98

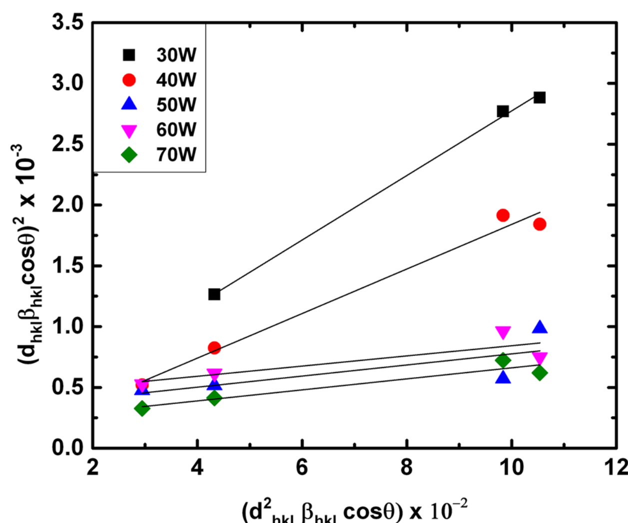

Fig. 3 Size–Strain (S–S) plots for NiO thin films deposited at different sputter powers

the kinetic energy of gas molecules is low and reactive oxygen gas molecules dominate during the growth process. On the other hand, at high sputter powers, the ejected atoms gain enough kinetic energy and eventually grown films exhibited better crystalline nature with a reduced surface roughness due to better agglomeration of the particles. We have found an inverse relationship between the surface roughness and the sputter power. The increased uniformity of the films at higher sputter powers could lead to such behavior.

4.3 Optical studies

Figure 5 shows the transmittance spectra of NiO thin films grown at different sputter powers. Initially, the grown films at 30W have shown a transmittance of 27% in the visible region. At lower sputter powers, kinetic energy of sputtered gas molecules is low and reactive oxygen gas molecules dominate during the growth process. In this scenario, deposited NiO films contain more number of oxygen interstitial defects; in other words, we can say that Ni^{+3} states are dominated over Ni^{+2} states which significantly reduces the transmittance of the film. As the sputter power progressively increased to 70 W, the average transmittance of the films increased to 72%. At higher sputter powers, the kinetic energy of the sputter gas molecules increases and it dominates that of the oxygen atoms during deposition process. Hence, we obtained the better sputtering yield at high sputtering power process. As a consequence, the measured transmittance of the film significantly increased as a function of sputter power, due to the presence of Ni^{+2} states predominating over Ni^{+3} states.

The fundamental optical absorption coefficient was evaluated by using transmittance spectra followed by relation.

$$\alpha = \frac{\left(\ln T^{-1}\right)}{d} \tag{9}$$

where α is the absorption coefficient, T is the transmittance spectra and d is the thickness of the film.

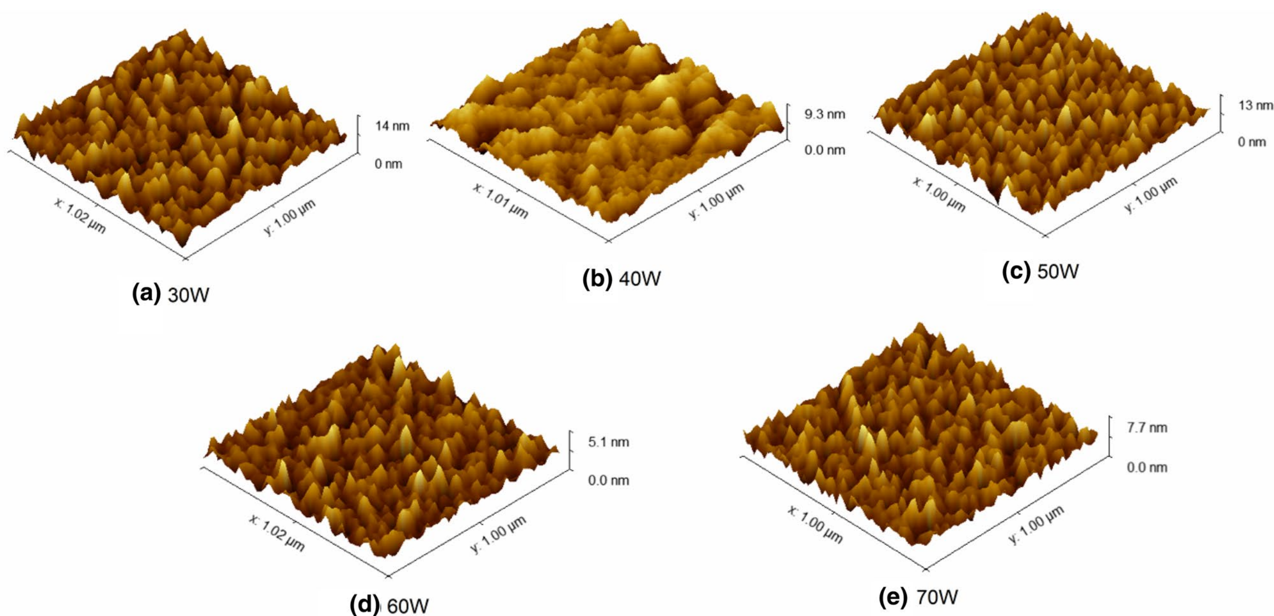

Fig. 4 AFM images of NiO thin films deposited at different sputter powers

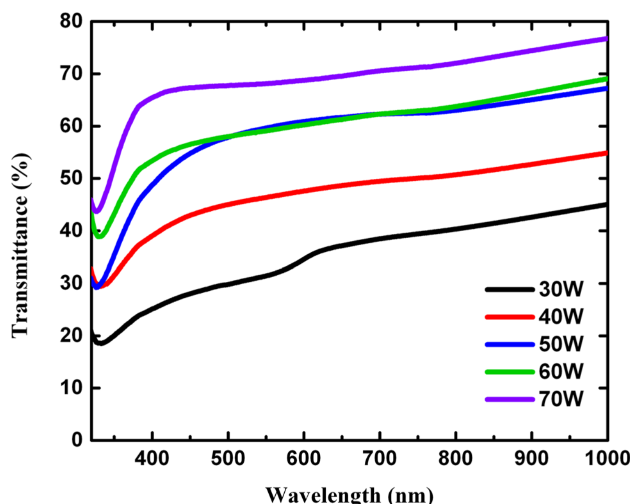

Fig. 5 Transmittance spectra of NiO thin films deposited at different sputter powers

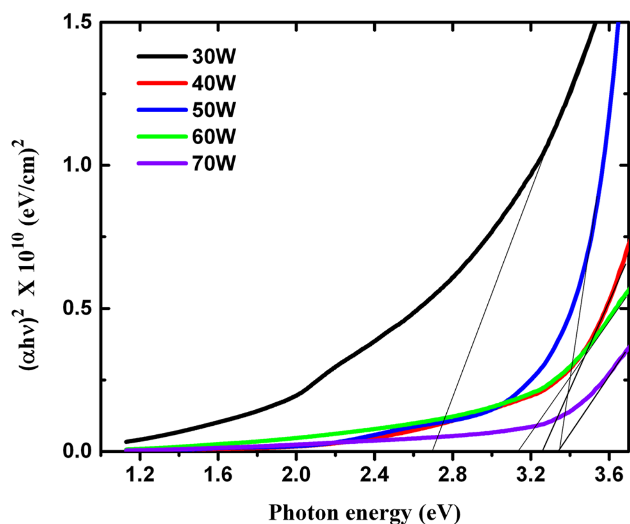

Fig. 6 Tauc plot of $(\alpha hv)^2$ versus (hv) of NiO thin films deposited at different sputter power

$$(ahv)^{\frac{1}{n}} = A\left(hv - E_g\right) \quad (10)$$

where A is a constant, hv is the photon energy and n decides the type of transition, n = $\frac{1}{2}$ for the direct band transition. We have estimated the optical band gap by Tauc plot approach. As shown in Fig. 6, the linear region of the plot between $(ahv)^2$ versus photon energy, and the extrapolation to abscissa gives the optical band gap. We have not observed a monotonous increase in the band gap with an increase in sputter power. In the present investigation, the estimated optical band gap varied from 2.70 eV to 3.34 eV for different sputter powers as shown in Fig. 6. At a sputter power of 30 W, a band gap of 2.70 eV was obtained. The XPS study reveal the presence of large number of defects lowering the energy band gap as well as transmittance of the film. The band gap exhibited an increasing trend from 2.70 eV to 3.34 eV, as the sputter power increased from 30 to 50 W. The deposited films at 60 W power exhibited a reduced band gap value, i.e., 3.14 eV. Such narrowing is related to the structure [23]. Moreover, the tensile strain present in the film also affects the band gap, and estimated strain values (extracted strain values from both W–H and S–S plots) are listed in Table 2. It can be noticed that larger optical band gap was close to the stoichiometry of the NiO thin film due to the presence of a minimum number of intrinsic defects. Therefore, larger tensile strain causes the lowering band gap of the film. Moreover, the variation of the band gap could also be due to stoichiometry of the film, surface morphology, structural properties, and defects states [23].

4.4 Chemical analysis (XPS)

To get a better understanding of the chemical composition, the presence of defects states and interaction between the metal–oxygen atoms of the NiO thin films is examined by X-ray photoelectronic spectroscopy (XPS). NiO material belongs to the transition metal oxide group and it is crucial to find the oxidation state. Generally, NiO exhibits spin–orbit doublet and its multiple peaks result in complicated line shape, and it is difficult to assign the oxidation state concerning binding energies.

Before proceeding toward the XPS spectrum, the carbon correction at 284.8 eV as a standard reference peak was applied in corrected wide spectra, Ni2p and O1s spectra. After carbon correction, survey spectrum elemental mapping has been carried out from 0 to 1200eV of binding energy (BE). For XPS characterization, we have considered NiO films grown at 30 W and 70 W of sputter power and their survey spectra are displayed in Fig. 7(a and b). It contained photoemission intensity peaks such as Ni3p, Ni3s, O1s, Ni2p$_{1/2}$,Ni2p$_{3/2}$, Auger electron peaks Ni LMM, O KLL as well as C1s peak was also identified [23]. We have observed that there was no foreign element present in wide spectra which indicated that grown film has a desired NiO composition during the sputtering process.

The Ni2p XPS spectrum was background corrected with Shirley type of background and deconvoluted by GL (Gaussian–Lorentzian) mode to extract the chemical composition. Ni2p spectra with two spin–orbit coupling spectra Ni2p$_{1/2}$, and Ni2p$_{3/2}$were designated at binding energy span of 850 to 869 eV and 870 to 885 eV, respectively. In this case, we have observed NiO complex main peaks, and their shakeup satellite peaks. Based on the binding energy of the sample, we have identified the peaks and assigned the oxidation states

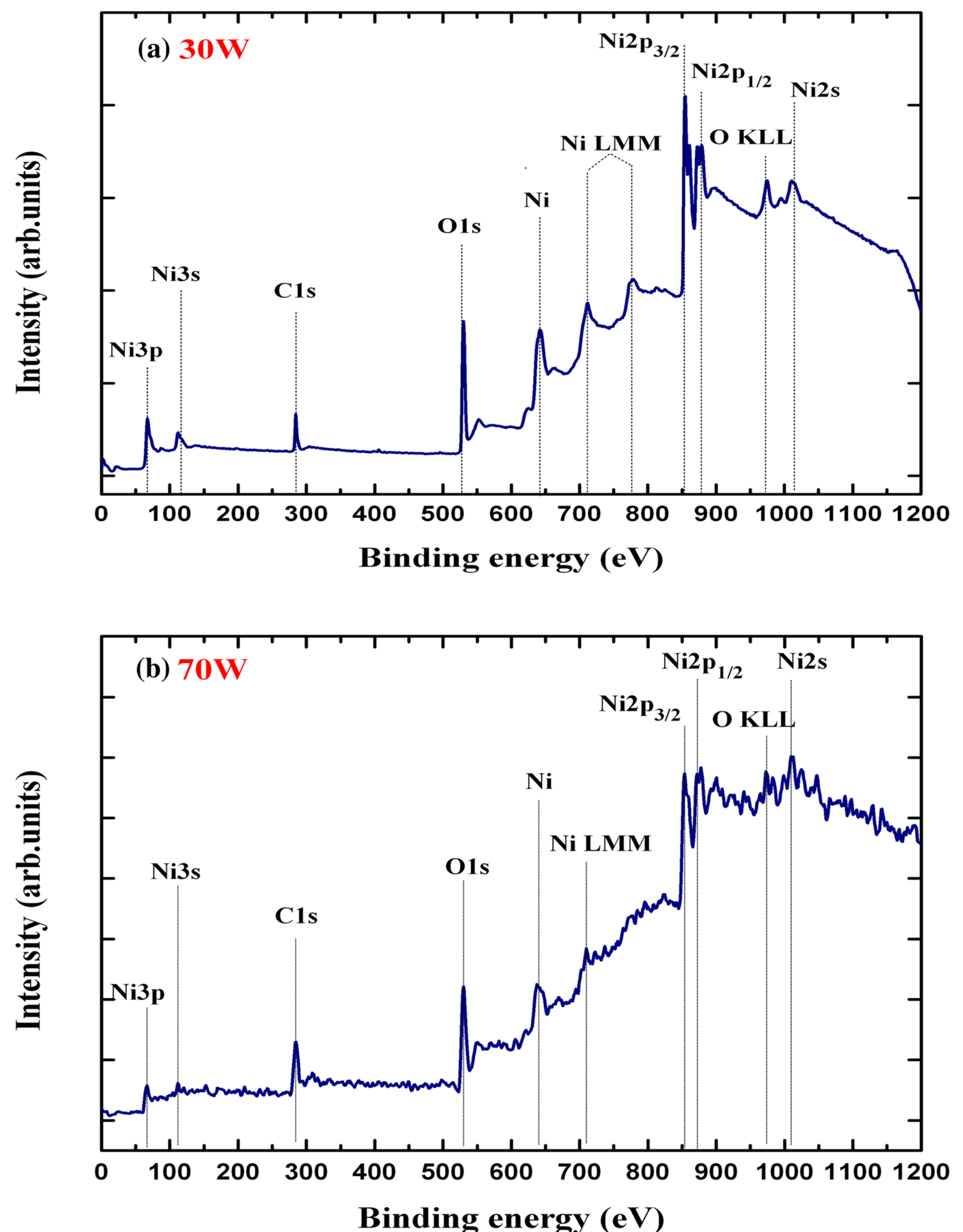

Fig. 7 Representative of XPS wide survey spectra of NiO thin films deposited at **a** 30 W and **b** 70W of sputter power

for both samples as shown in Fig. 8(a and b). The estimated chemical compositions are given in Tables 3 and 4.

The broadening of the main peak and its shakeup satellite peaks mainly depends on the interaction between the nickel and oxygen atoms. Therefore, the number of satellite peaks usually arises in the higher BE of the $Ni2p_{3/2}$, and $Ni2p_{1/2}$ and are dominating due to the mixing of d–d transition and increased Ni3d-O2p hybridization. The separation between the $Ni2p_{1/2}$, and $Ni2p_{3/2}$binding energy peak intensity range from 17.39 to 17.40 eV [24, 25]. The presence of $Ni2p_{1/2}$, and $Ni2p_{3/2}$spectrum binding energy difference is evident of the dependency of the sputter power and reactive oxygen gas on the chemical structure of the grown film. We observed a minor chemical shift which occur both in the Ni2p spectra and O1s spectra. It may be due to binding energy charging effect, which is caused due to changes or variation in ionic charge peaks due to changes in their broadening and its chemical concentration due to cation vacancy induced by the oxygen [26].

Many researchers have interpreted the XPS spectra of NiO thin films, which were prepared by different routes that include chemical as well as physical methods. The chemical composition and binding energy peaks of different oxidation states marginally vary based on the preparation parameters and post-annealing treatment. K.S. Kim et al. have observed three main peaks at 854 eV, 855.8 eV and

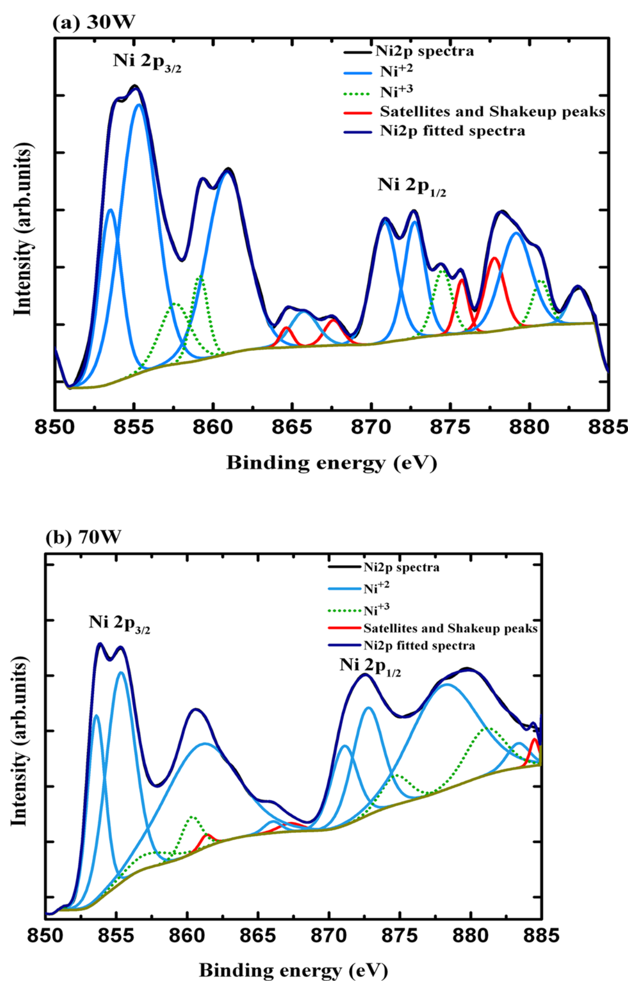

Fig. 8 Ni 2p X-ray photoelectron spectroscopy (XPS) NiO thin films deposited at **a** 30 W and **b** 70W of sputter power

861.2 eV for $Ni2p_{3/2}$spectra, while O1s peak assigned at 529.1 eV suggested a pure stoichiometric NiO. The oxidation process of the same sample indicated that $Ni2p_{3/2}$ spectrum contain peak located at 855.9 eV, 861.4 eV and their O1s spectra reflected at 530.9 eV indicate the presence of Ni_2O_3 phase [27]. Sasi et al. reported NiO films prepared by pulsed laser deposition on quartz substrates. They observed a transformation mechanism upon annealing with the presence of NiO phase followed by Ni_2O_3phase. The Ni_2O_3 phase was found at 856.5 eV, 862 eV, 873.7 eV and 880 eV. Similarly, NiO phase contain the following peaks: 855.1 eV, 861.9 eV, 873.2 eV, 880.4 eV. A marginal shift in the O 1 s spectrum from 529.47 eV to 529.82 eV was reported [28]. Dong-Soo Kim et al. reported NiO films deposited on SiO_2/Si substrates by RF reactive sputtering. Ni2p XPS spectra confirmed BE peak positions at 854.5 eV, 856 eV, 861.5 eV, 873 eV and 879.8 eV assigned to the Ni^{2+} state. Similarly, the peaks at 856.1 eV and 861.7 eV assigned to Ni^{3+}state [29]. Jung Kyu Kim observed multiple peaks of Ni^{2+}state-assigned at 854.1 eV and 872 eV. Similarly, BE peaks of 856.1 eV and 873.9 eV represent Ni^{3+}state in the non-stoichiometric NiO thin films [30]. Overall, our XPS results strongly match with the earlier reported results and the consolidated table contains quantification of chemical states listed in Tables 3 and 4.

At 30 W sputtering process, the interaction between the Ni^{2+} and O^{2-} is in balanced in the Ar: O_2 atmosphere. As a result, the concentration of the nickel vacancy is more compared to the oxygen atoms in the films, resulting in excess defects in the NiO film. Meanwhile, XPS confirms that Ni^{3+} state is dominant in these films. With increasing sputter power at a step of 10 W, Ni^{2+}dominated over Ni^{3+}indicating that metallic nature of the film significantly decreases with increasing sputter power. Thus, deposited films at 30 W of sputter power resulted in a number of Ni^{3+}ions that leads to the formation of Ni vacancies. NiO ascribed as Ni^{2+}oxidation state with their surface area atomic percentage in the range 79.75 to 86.75% for the films deposited with sputter powers in the range 30 to 70 W, respectively. This variation in the atomic percentage lead to the variation in resistivity and carrier concentration in the films. The stoichiometric ratio $\frac{Ni}{O}$ has been estimated from the chemical composition of the Ni^{3+}state and it marginally decreased from 1.15 to 0.86 with increased sputter power which indicates that excess of defects state has reduced. Estimated defect ratio between the $\frac{Ni^{3+}}{Ni^{2+}}$ imply that defect state has fallen from 16.38 to 13.31% as a function of sputter power. It indicates that growing film at higher powers removes the unwanted oxygen defects and enhancing the lattice–oxygen interaction.

Figure 9 (a and b) depicts the individual deconvoluted core level O1s XPS spectra, and their peaks are distinguished based on the binding energies. The center peak at 529.2 eV BE core-level O1s spectra assigned as nickel and oxygen lattice bonding. While 530.8 eV BE peak ascribed as nickel vacancy or deficiency, which is mainly responsible for creating vacancy of NiO thin film in terms of Ni^{3+}ion-induced on the surface of the film. In addition, a small peak situated at 531.9 eV represents the O–H group and another tiny peak is also found at 533.5 eV, which could be assigned to the absorbed oxygen molecules [31–33].

The resistivity of NiO film significantly increases due to the reduction in Ni^{3+}ions. That means the process of vacant positions of Ni^{2+}ions occupied by Ni^{3+}cations during the deposition. Moreover, modulation of the electrical properties largely depends on the stoichiometry in the samples. We have noticed that grown NiO thin films at low sputter powers are influenced with a greater number of Ni vacancies. According to Kroger–Vink notation, nickel vacancies are created owing to neighboring two Ni^{2+}ionized to $Ni^{3+}$by contributing an extra electron to oxygen. The following equation governs the vacancies:

Table 3 XPS quantification for NiO thin films deposited at 30 W and 70 W of sputter powers

Sputter power (W)	Ni $2p_{3/2}$ Spectral features				Ni $2p_{1/2}$ Spectral features			
	Binding energy (eV)	FWHM (eV)	Atomic (%)	Peak assignment	Binding energy (eV)	FWHM (eV)	Atomic (%)	Peak assignment
30	853.53	1.69	10.08	Ni^{+2}	870.92	1.89	7.78	Ni^{+2}
	855.27	2.74	25.19	Ni^{+2}	872.73	1.56	6.18	Ni^{+2}
	857.40	2.23	4.62	Ni^{+3}	874.50	1.38	3.06	Ni^{+3}
	859.34	1.21	3.51	Ni^{+3}	875.72	0.95	1.73	Satellite, shakeup
	860.88	3.03	18.83	Ni^{+2}	877.78	1.48	3.69	Satellite, shakeup
	864.63	0.92	0.63	Satellite, shakeup	879.04	2.32	7.49	Ni^{+2}
	865.74	2.03	2.42	Ni^{+2}	880.81	1.22	1.88	Ni^{+3}
	867.61	1.34	1.15	Satellite, shakeup	883.05	1.39	1.78	Ni^{+2}
70	853.58	1.48	9.53	Ni^{+2}	870.98	2.18	5.96	Ni^{+2}
	855.29	2.42	17.63	Ni^{+2}	872.73	2.53	9.32	Ni^{+2}
	857.31	3.82	1.85	Ni^{+3}	874.66	2.37	2.38	Ni^{+3}
	859.69	1.66	2.11	Ni^{+3}	878.20	5.60	20.10	Ni^{+2}
	860.89	6.11	22.08	Ni^{+2}	881.04	3.25	5.21	Ni^{+3}
	861.33	1.00	0.42	Satellite, shakeup	883.35	1.85	1.56	Ni^{+2}
	865.90	1.44	0.57	Ni^{+2}	884.50	0.74	0.67	Satellite, shakeup
	867.27	2.00	0.57	Satellite, shakeup				

Table 4 Extracted chemical properties of NiO thin films XPS O1s spectra

O1s Spectral features of 30 W				O1s Spectral features of 70 W			
Binding Energy (eV)	FWHM (eV)	Atomic (%)	Peak assignment	Binding Energy (eV)	FWHM (eV)	Atomic (%)	Peak assignment
529.25	1.257	53.96	Ni^{2+}	529.27	1.872	86.71	Ni^{2+}
530.84	1.323	32.96	Ni^{3+}	530.88	1.775	13.29	Ni^{3+}
531.94	1.588	11.35	O–H				
533.55	0.640	1.72	Adsorbed Oxygen				

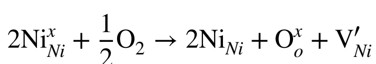

$$2Ni_{Ni}^{x} + \frac{1}{2}O_2 \rightarrow 2Ni_{Ni}^{\cdot} + O_o^{x} + V_{Ni}^{\prime}$$

where Ni_{Ni}^{x}, $Ni_{Ni}^{\cdot}$, $V_{Ni}^{\prime}$, O_o^{x} stands for Ni^{2+}, Ni^{3+}, the ionized Nickel vacancy and O^{2-} ions, respectively.

The p-type conductivity in these films is due to nickel vacancy and oxygen interstitials in the NiO crystal lattice. Generally, these holes act as a quasi-localized in the Ni^{2+} vacancy served as an acceptor in top of the valence band [29].

At lower sputter powers, the sputtering yield is too small, whereas growing complete stoichiometry of NiO thin film is uneasy. This is believed to be due to the influence of oxygen atoms dominating over sputter gas at lower powers. Besides, the sputter gas does not get enough kinetic energy to involve the process, so that excess metal vacancies prevailed at low sputter powers. As evident from atomic percentage, the defect density is enhanced and splitting occur at higher binding energy in the spectra since reactive oxygen play vital role that leads to the formation of low resistive films. Further, as shown in Fig. 9b, grown NiO films at higher sputter power does not have the unwanted oxygen defects and it enhanced the Ni – O or metal–oxygen lattice along with crystallinity of the film.

4.5 Raman spectroscopy analysis

Figure 10 depicts the Raman spectra of NiO thin films grown with different sputter powers at room temperature. The main band positions and associated modes have been identified in the Raman spectra of NiO film grown at 50 W of sputter power, which is shown as inset of Fig. 10. In the characteristics of Raman spectra at lower sputter powers such as 30 W and 40 W, only TO and LO modes have been identified, and it could be due to the poor formation of crystallite sizes. The first-order transverse modes TO and TO′ were situated at 398 cm^{-1} and 472 cm^{-1}, respectively, and first-order longitudinal modes, LO and LO′ were situated at 579 cm^{-1} and

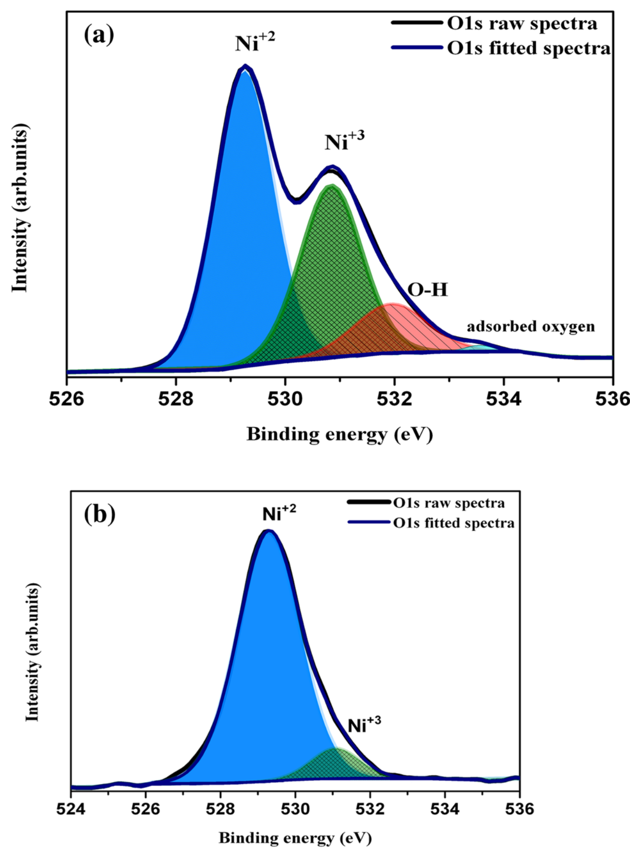

Fig. 9 O1s X-ray photoelectron spectroscopy (XPS) NiO thin films deposited at **a** 30 W and **b** 70 W of sputter power

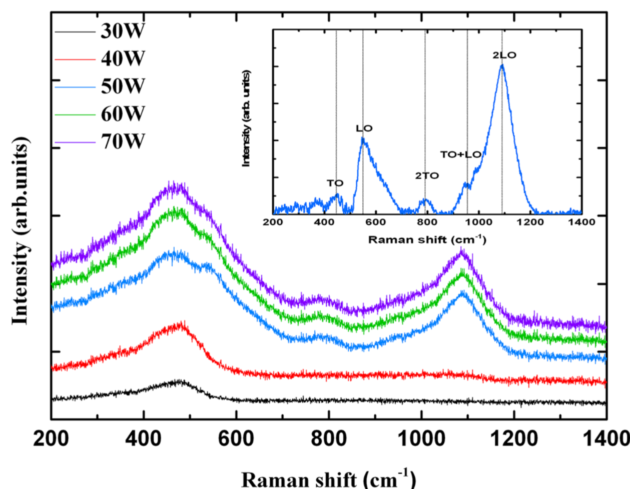

Fig. 10 Raman spectra of NiO thin films grown at different sputter powers (Inset: after baseline correction vibration modes identified NiO film grown at 50 W of sputter power)

665 cm^{-1} which indicate the presence of Nickel defects, i.e., Ni^{3+} ions exists in the NiO film and their existence is also confirmed by the XPS characterization [34]. The stronger second-order transverse and longitudinal mode located at 821 cm^{-1} and 1119 cm^{-1} represents a 2TO and 2LO in the inset of Fig. 10. The combination of TO + LO phonon excitation mode assigned at 979 cm^{-1} in the NiO film. With an increase in the crystallite size, the 2LO and 2TO peak appeared in the spectra of the NiO film grown at 50 W of power. Longitudinal modes LO and 2LO reveal a strong interaction between the nickel and oxygen bonding [24]. In this analysis, we have observed that there is a small shift in the spectra due to the presence of strain in the film, and it is worth noting that the contribution from the glass substrate is also not ruled out.

4.6 Electrical properties

Figure 11 (a–c) represents the variation of electrical properties of the NiO thin films grown under different sputter powers. The films have shown p-type conductivity as examined by van der Pauw technique. It was observed that resistivity of the films grown at 30 W was 8.37 Ω-cm, and it increased to 4.81×10^2 Ω-cm for films deposited at 70 W of sputter power. At low sputter powers, the reaction between the combined Ar : O_2 ambience with the nickel target is insufficient. It resulted in high concentration of nickel vacancies in the film causing p-type conductivity. Therefore, resistivity of the film increased with sputter power due to increased average crystallite size. The larger crystallite size means less grain boundary scattering, which enhances the transmittance and increase in the resistivity of the NiO thin films. This could also be due to the reduced Ni^{3+}ions over Ni^{2+}ions.

The non-stoichiometric NiO thin film carrier concentration varied about three orders in of the range 10^{17} to 10^{14} cm^{-3}. Most importantly, it can be found that the highest electrical mobility of 84.56 cm^2V^{-1} s^{-1} was achieved at 70 W, and it is marginally reduced to 7.46 cm^2V^{-1} s^{-1} at 30 W of power as shown in Fig. 11c. The significant variation of carrier mobility is due to the colloidal kinetic energy loss of the particles in the sputtering process. Because of the collisions among the carriers, the carrier mobility has reduced at lower sputter powers [35].

It can be observed that crystallites size was minimum for the deposited films at 30 W. We have noticed a better formation of crystallite size with increasing sputter power. To get an insight, we have analyzed our XPS data. There was an evidence from NiO XPS spectra that the presence of $Ni^{3+}$is in excess in the low sputtered films. While increasing sputter power, $Ni^{2+}$is predominant over Ni^{3+}ions, which implies that the metallic nature of the film significantly increases. It can be observed that carrier mobility of the films increases with the sputter power because of the better

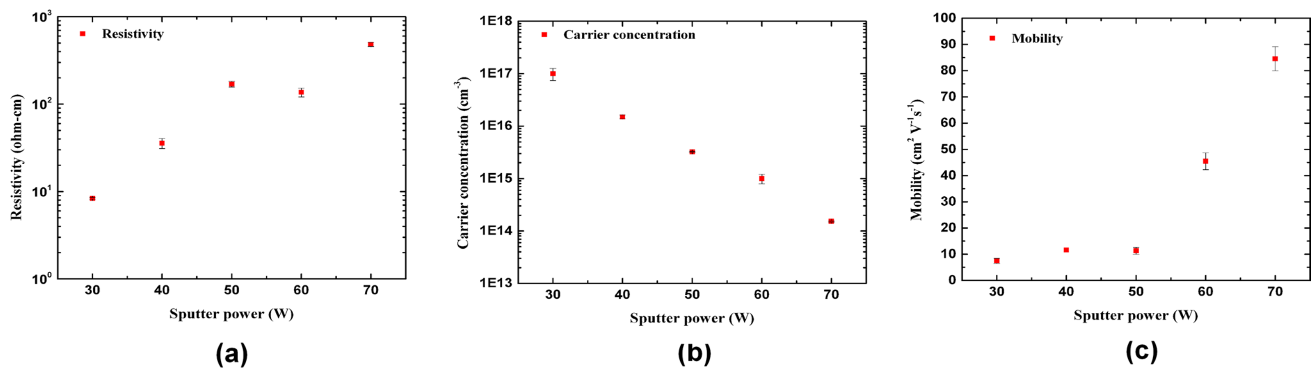

Fig. 11 Electrical properties of NiO thin films at different sputter powers. **a** Electrical resistivity **b** Carrier concentration and **c** Mobility

crystalline nature and the presence of minimum number of defects. Generally, TCO films exhibit larger grain boundary with the small particles size causing scattering of carriers. At lower sputter powers, we have found a decreasing mobility due to the poor crystallization which reduces the carrier movement because of intrinsic defects present in the grown films. The variation in the NiO stoichiometry in the grown films causes the increase in electrical resistivity. Therefore, it can be observed that both structural and chemical properties strongly impact the transport properties. The electrical properties of NiO thin films are strongly associated with the stoichiometry of the compound, presence of defects, and microstructure [36]. Besides, the variability of electrical properties can also rely on other processing parameters such as oxygen partial pressure and sputter pressure. Overall, by governing these variables, it is feasible to tune the properties for desired applications. Among all the films, the films grown at 70 W power exhibited lower carrier concentration with high mobility, and they are well-suitable for the thin film transistor applications.

5 Conclusions

To summarize, the investigated physical properties of NiO thin films depend on sputter power. The X-ray diffraction results show polycrystalline orientations with FCC phase on NiO films with predominant (111) peak, the intensity of which increased with an increase in sputter power. Estimated average crystallite size by three different methods have shown a better crystallinity for the films grown at higher sputter powers, and all films exhibited tensile strain in the films. Optical transmittance significantly increased with an increase in crystallite size, and the estimated band gap increased from 2.70 eV to 3.34 eV as the sputter power increased from 30 to 70 W. Ni2p X-ray photoelectron spectroscopy confirms the presence of both Ni^{2+} and Ni^{3+} defect states, of which Ni^{3+} state significantly plays a role in structural and electrical properties. Raman vibrational modes attributed to the enhanced crystallite size and existence of strain in the films. It was found that electrical resistivity varied from 8.37 to 4.81×10^2 Ω-cm and carrier hole mobility significantly increased from 7.46 $cm^2V^{-1}s^{-1}$ to 84.56 $cm^2V^{-1}s^{-1}$with increase in sputter power. The choice of sputter power with the combination of argon and oxygen ratio for metal oxide films could get some interesting results that will be beneficial for numerous applications.

Acknowledgements Parashurama Salunkhe thank to Manipal Academy of Higher education for financial support under the Dr.T.M.A. Pai PhD scholarship scheme. We would like to thank Micro- and Nano-characterization Facility (MNCF) at CeNSE, funded by the Ministry of Electronics and Information Technology (MeitY), Government of India, Indian Institute of Science (IISc), Bengaluru.

Funding Open access funding provided by Manipal Academy of Higher Education, Manipal.

Declarations

Conflicts of interest There are no conflicts of interest to declare.

Open Access This article is licensed under a Creative Commons Attribution 4.0 International License, which permits use, sharing, adaptation, distribution and reproduction in any medium or format, as long as you give appropriate credit to the original author(s) and the source, provide a link to the Creative Commons licence, and indicate if changes were made. The images or other third party material in this article are included in the article's Creative Commons licence, unless indicated otherwise in a credit line to the material. If material is not included in the article's Creative Commons licence and your intended use is not permitted by statutory regulation or exceeds the permitted use, you will need to obtain permission directly from the copyright holder. To view a copy of this licence, visit http://creativecommons.org/licenses/by/4.0/.

References

1. T.S. Tripathi, M. Karppinen, Adv. Mater. Interfaces **4**, 1 (2017)
2. Z. Wang, P.K. Nayak, J.A. Caraveo-Frescas, H.N. Alshareef, Adv. Mater. **28**, 3831 (2016)
3. V. Manjunath, S. Bimli, K.H. Parmar, P.M. Shirage, R.S. Devan, Sol. Energy **193**, 387 (2019)
4. J. Robertson, R. Gillen, S.J. Clark, Thin Solid Films **520**, 3714 (2012)
5. C.W. Dhananjay, C.W. Chu, M.C. Ou, Z.Y. Wu, K.C. Ho, S.W. Lee, Appl. Phys. Lett. **92**(1), 232103 (2008)
6. C.R. Gobbiner, A.V.M. Ali, D. Kekuda, J. Mater. Sci. Mater. Electron. **26**, 9801 (2015)
7. X. Zhao, J. Chen, N.G. Park, Solar RRL **3**, 1 (2019)
8. H. Sato, T. Minami, S. Takata, T. Yamada, Thin Solid Films **236**, 27 (1993)
9. A. Liu, H. Zhu, Z. Guo, Y. Meng, G. Liu, E. Fortunato, R. Martins, F. Shan, Adv. Mater. **29**, 1 (2017)
10. S. Nandy, B. Saha, M.K. Mitra, K.K. Chattopadhyay, J. Mater. Sci. **42**, 5766 (2007)
11. A.M. Soleimanpour, A.H. Jayatissa, G. Sumanasekera, Appl. Surf. Sci. **276**, 291 (2013)
12. K.X. Steirer, J.P. Chesin, N.E. Widjonarko, J.J. Berry, A. Miedaner, D.S. Ginley, D.C. Olson, Org. Electron. **11**, 1414 (2010)
13. A.A. Al-Ghamdi, M.S. Abdel-Wahab, A.A. Farghali, P.M.Z. Hasan, Mater. Res. Bull. **75**, 71 (2016)
14. D. Kawade, S.F. Chichibu, M. Sugiyama, J. Appl. Phys. **116**, 1 (2014)
15. P.S. Patil, L.D. Kadam, Appl. Surf. Sci. **199**, 211 (2002)
16. V.P. Patil, S. Pawar, M. Chougule, P. Godse, R. Sakhare, S. Sen, P. Joshi, J. Surf. Eng. Mater. Adv. Technol. **01**, 35 (2011)
17. Y.M. Lu, W.S. Hwang, J.S. Yang, H.C. Chuang, Thin Solid Films **420–421**, 54 (2002)
18. Y. Wang, J. Ghanbaja, F. Soldera, P. Boulet, D. Horwat, F. Mücklich, J.F. Pierson, Phys. Status Solidi - Rapid Res. Lett. **12**, 1 (2018)
19. A. Karpinski, A. Ferrec, M. Richard-Plouet, L. Cattin, M.A. Djouadi, L. Brohan, P.Y. Jouan, Thin Solid Films **520**, 3609 (2012)
20. H.L. Chen, Y.S. Yang, Thin Solid Films **516**, 5590 (2008)
21. T. Potlog, L. Ghimpu, V. Suman, A. Pantazi, M. Enachescu, Mater. Res. Express **6**, 096440 (2019)
22. D. Nath, F. Singh, R. Das, Mater. Chem. Phys. **239**, 122021 (2020)
23. M. Becker, F. Michel, A. Polity, and P. J. Klar, Physica Status Solidi (B) Basic Research. **255**(1) (2018)
24. P. Salunkhe, M. A. A V, and D. Kekuda, Materials Research Express. **7(1)**, 016427 (2020)
25. G. George, S. Anandhan, RSC Adv. **4**, 62009 (2014)
26. M.W. Roberts, R.S.C. Smart, J. Chem. Soc. Faraday Trans. 1: Phys. Chem. Condens. Phases **80**, 2957 (1984)
27. K.S. Kim, N. Winograd, Surf. Sci. **43**, 625 (1974)
28. B. Sasi, K.G. Gopchandran, Nanotechnology **18**, 115613 (2007)
29. D. Soo Kim and H. Chul Lee, Journal of Applied Physics. **112**(1), (2012)
30. J.K. Kim, Polymers **11**, 120 (2019)
31. R. Islam, G. Chen, P. Ramesh, J. Suh, N. Fuchigami, D. Lee, K.A. Littau, K. Weiner, R.T. Collins, K.C. Saraswat, ACS Appl. Mater. Interfaces. **9**, 17201 (2017)
32. M. Morales-Luna, M.A. Arvizu, M. Pérez-González, S.A. Tomás, J. Phys. Chem. C **123**, 17083 (2019)
33. M. Ponce-Mosso, M. Pérez-González, P.E. García-Tinoco, H. Crotte-Ledesma, M. Morales-Luna, S.A. Tomás, Catal. Today **349**, 150 (2020)
34. M. Marciuš, M. Ristić, M. Ivanda, S. Musić, J. Alloy. Compd. **541**, 238 (2012)
35. P. S. R. Y. Ashok Kumar Reddy, A. Mallikarjuna Reddy, A. Sivasankar Reddy, **4**, 4 (2012).
36. M. Predanocy, I. Hotový, M. Čaplovičová, Appl. Surf. Sci. **395**, 208 (2017)

Publisher's Note Springer Nature remains neutral with regard to jurisdictional claims in published maps and institutional affiliations.